Fachtagung "Experimentelle Strömungsmechanik"
6. – 8. September 2016, Cottbus

PIV Messungen einer Schlitzfilmkühlung mit Stoßinteraktion

PIV measurements of slot-film cooling at shock interaction

Pascal Marquardt[1], Michael Klaas[1], Wolfgang Schröder[1]
[1]Institute of Aerodynamics, RWTH Aachen University, 52062 Aachen, Germany,
corresponding author p.marquardt@aia.rwth-aachen.de

Schlitzfilmkühlung, Stoß/Kühlfilm Interaktion, Überschallströmung, High-speed PIV
slot-film cooling, shock/cooling-film interaction, supersonic flow, high-speed PIV

Abstract

Supersonic slot-film cooling is a promising cooling concept for surface temperature reduction of engine components that experience high thermal loads. If shocks are present, their interaction with the cooling film may change the fundamental structure of the flow field in the vicinity of the surfaces that require cooling, which in turn can reduce the cooling effectiveness. The scope of this study is to analyze the influence of an impinging shock on a cooling-film flow with an injection Mach number of $Ma_i = 1.8$. The cooling film is injected beneath a turbulent boundary layer through a two-dimensional slot nozzle at a freestream Mach number of $Ma_\infty = 2.45$. A flow deflection of $\beta = 5°$ generates a shock wave which impinges upon the cooling film. The flow field of the shock/cooling-film interaction is investigated by means of high-speed particle-image velocimetry and the time-averaged velocity fields and the Reynolds shear stress distributions are analyzed for a flow with and without shock interaction. The results show a transition of the laminar slot boundary layer caused by the lip-expansion waves and the lip shock. With shock interaction, the turbulent mixing downstream the shock impingement position is significantly enhanced and the cooling-film flow relaxes faster towards a boundary layer flow.

Introduction

In supersonic applications with high thermal loads, e.g., scramjet combustors, supersonic film cooling through two-dimensional slots is a promising cooling concept for surface temperature reduction (Juhany & Hunt 1994, Konopka et al. 2012, 2013a). However, if shocks that interfere with the cooling film occur, a locally reduced cooling effectiveness might be the consequence.
Figure 1 shows the basic structure of the flow field of a tangential film-cooling configuration that is not influenced by an impinging shock wave (Konopka et al. 2012). According to Seban & Back (1962) and Juhany (1994), the flow field can be divided into three regions. The first region is the potential-core region right downstream of the injection, which is bounded by the mixing layer that emanates from the lip and the slot-flow boundary layer. In this region, the cooling effectiveness is unity. The potential-core region ends where the mixing layer and the slot-flow boundary layer merge and form the so-called wall-jet region that is characterized by intense mixing. Further downstream, the flow relaxes to that of an undisturbed turbulent boundary layer. Consequently, this region is called boundary-layer region.

Karlsruhe, Germany, ISBN 978-3-9816764-2-6

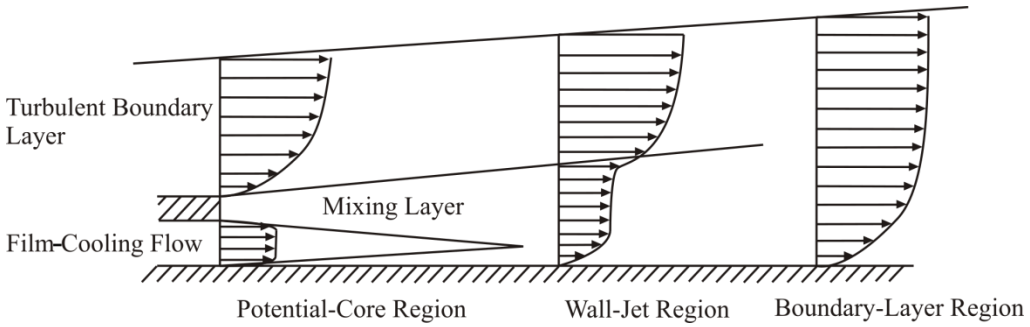

Fig. 1: Flow schematic with velocity profiles indicating the three distinct flow regions (Seban 1962, Juhany 1994) in a tangential film cooling configuration (Konopka et al. 2012).

The wall heat flux and, thus, the cooling effectiveness might change dramatically in the event that a shock impinges on the cooling film. However, in the literature contradictory results are reported concerning the extent of this change. Alzner & Zakkay (1971) performed experimental investigations of a shock/cooling-film interaction in an axisymmetric flow at a freestream Mach number of $Ma_\infty = 6$ with sonic injection. The shock was generated by an axisymmetric wedge around an axisymmetric centerbody with a flow deflection of 10°. The measurement of the heat transfer distribution showed a distinct reduction of the peak heat flux due to the injected cooling film. Experimental and numerical studies of a helium injection into a turbulent boundary layer at a freestream Mach number of $Ma_\infty = 6.4$ were conducted by Kamath et al. (1990). The cooling film was injected with an injection Mach number of $Ma_i = 3$. The shocks impinging on the cooling film were generated by flow deflections of 5.5°, 8°, and 10.5°. The Reynolds-averaged Navier Stokes simulations (RANS) and the measurements of the wall heat flux indicated a small reduction of heat flux by the cooling film. Holden et al. (1990) performed experiments in a shock tunnel at a freestream Mach number of $Ma_\infty = 6$ and injection with an injection Mach number of $Ma_i = 3$. Shocks generated by either a 10°, 15°, or a 20° flow deflection impinged upon the cooling film. Contradictory to Alzner & Zakkay (1971) the authors found that film cooling has little or no effect on the peak heat transfer. Olsen et al. (1990) conducted experimental investigations of a helium injection with an injection Mach number of $Ma_i = 3$ into a turbulent boundary layer at a freestream Mach number of $Ma_\infty = 6.4$. They found that the shock impingement position has no effect on the peak heat flux. However, the authors did not state in which flow region, i.e., potential-core, wall-jet, or boundary-layer region the measurements were performed. Juhany & Hunt (1994) concluded that the differences in the results arise from the flow region where the shock impinges upon the cooling film. While Alzner & Zakkay (1971) investigated an interaction directly downstream of the injection point, Holden et al. (1990) analyzed a shock impingement 60 - 90 nozzle heights downstream of the injection. Juhany & Hunt (1994) investigated experimentally a shock/cooling-film interaction in the wall-jet region and in the boundary layer region with injection Mach numbers of $Ma_i = 1.2$ and 2.2 at a freestream Mach number of $Ma_\infty = 2.44$. They found a weak impact of the shock interaction on the temperature at the wall as long as no separation occurs. Kanda et al. (1996, 1997) performed experiments with sonic injection into a boundary layer at a freestream Mach number of $Ma_\infty = 2.35$. The shocks possessed a pressure ratio of either $p_2 / p_1 = 1.21$ or 1.44. They concluded their measurements by stating that mixing between the cooling flow and the freestream was not significantly increased by shock interaction.

Konopka et al. (2012, 2013b) performed large-eddy simulations (LES) of shock/cooling-film interaction in the potential-core region and the boundary-layer region for injection Mach numbers of $Ma_i = 1.2$ and 1.8. They found a shock induced decrease of the cooling effec-

Karlsruhe, Germany, ISBN 978-3-9816764-2-6

tiveness in all examined cases. However, the amount of the reduction in cooling effectiveness depends of the Mach number and the impingement position. The low Mach number case shows a stronger decrease with shock impingement in the boundary layer region, whereas the high Mach number case exhibits a higher cooling effectiveness decrease with shock interaction in the potential-core region.
The goal of this study is to analyze the effect of an oblique shock impinging upon a supersonic cooling film flow in the potential-core region. The cooling film is injected tangentially at an injection Mach number of $Ma_i = 1.8$ through a two-dimensional slot nozzle into a supersonic turbulent boundary layer with a freestream Mach number of $Ma_\infty = 2.45$. An oblique shock generated by a flow deflection of $\beta = 5°$ impinges upon the cooling film approx. 15 nozzle heights downstream of the injection. This parameter configuration corresponds to the parameters investigated by Konopka et al. (2013b). The flow field is investigated in detail by high-speed PIV measurements, and the mean flow field as well as turbulence statistics are analyzed and compared for cases with and without shock interaction.

Experimental Setup

Wind tunnel and model

All experiments have been conducted in the trisonic wind tunnel which is an intermittent working vacuum storage tunnel that is able to provide flows at Mach numbers ranging from 0.3 to 4.0. The unit Reynolds number varies between $6 \cdot 10^6$ and $16 \cdot 10^6$ m^{-1} depending on the Mach number and the ambient conditions. The freestream Mach number Ma_∞ in the test section is calculated from the pressure ratio p/p_0. The static pressure p is measured via pressure taps in the test section side walls during each run of the wind tunnel. The total pressure p_0 is measured with the same transducer just before each test run. The measurement error of the pressure transducer introduces an uncertainty in the Mach number determination of ±1.3%.

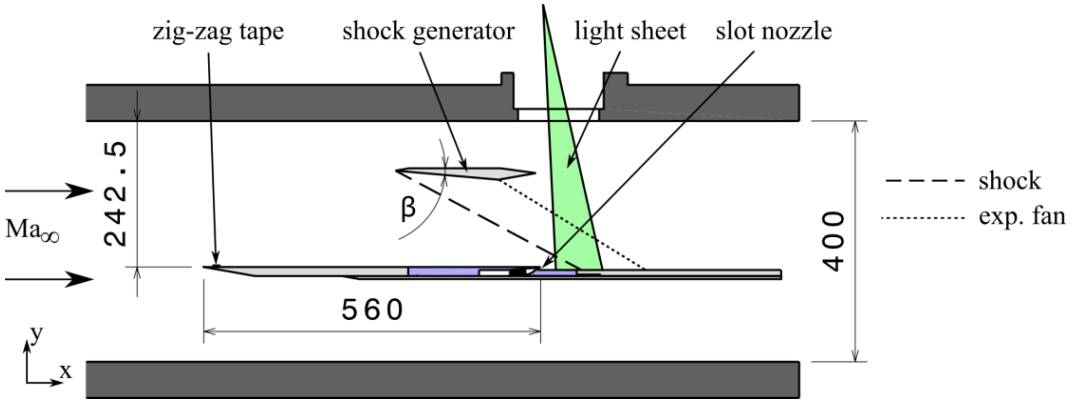

Fig. 2 Dimensions of the wind tunnel model and its location in the test section.

The model, mainly made of aluminum, spans across the entire 400 mm x 400 mm test section of the wind tunnel, has an overall length of 960 mm, and possesses a thickness of 20 mm. The dimensions of the model and its position in the test section are sketched in figure 2. The incoming flow is tripped by a 0.2 mm thick zigzag tape 10 mm downstream of the wedge-shaped leading edge of the model to ensure a uniform turbulent boundary layer at the position of injection. The cooling film is injected 560 mm downstream of the leading edge of the model through a 200 mm wide centered slot nozzle and develops along a 400 mm long flat plate. The oblique shock is generated by a wedge with a flow deflection angle of $\beta = 5°$.

Karlsruhe, Germany, ISBN 978-3-9816764-2-6

As the model, the wedge spans the entire test section width. The expansion fan emanating from the shock generator reaches the model 120 mm downstream of the shock impingement location.
An interchangeable nozzle insert allows to change the injection Mach number without dismounting the model from the test section. The injection flow enters the nozzle insert symmetrically from both sides through rectangular ducts. Corner vanes inside the plenum chamber deflect the cooling flow by 90° into the main flow direction and smoothly adapt the cross-section areas between the inlets and the outlet to avoid flow separation inside the plenum. Before the flow is accelerated to the injection Mach number, it is guided through a honeycomb flow straightener with a cell size of 1.6 mm and a length of 28 mm. The flow straightener is inclined by an angle of 5° to reduce the amount of tracer particles impacting on the bottom part of the nozzle. Static pressure and temperature of the cooling film are monitored via a pressure tap and a thermocouple downstream of the flow straightener. Upstream of the flow straightener, two struts are installed to avoid a deformation of the nozzle insert due to the increased pressure inside the plenum chamber. The supersonic part of the Laval nozzle is designed as a symmetric, bell-shaped nozzle with an exit height of S = 4 mm and a lip thickness of 1 mm. A spanwise and a streamwise cross section of the nozzle insert with the plenum chamber is depicted in figure 3.

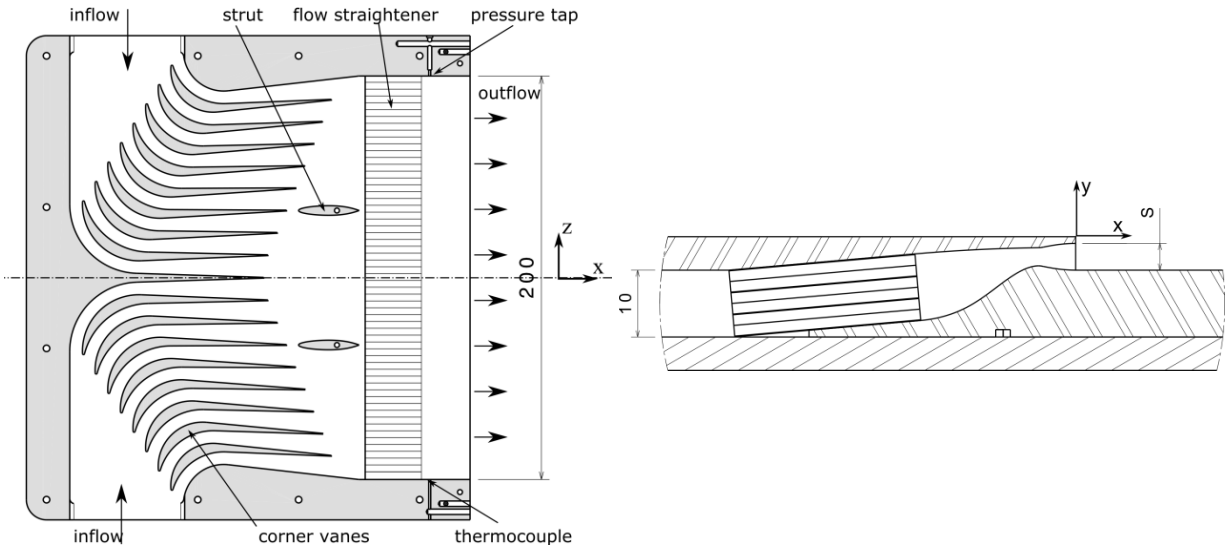

Fig. 3: Spanwise cross section of the nozzle insert with plenum (left) and streamwise cross section of the slot nozzle for an injection Mach number of $Ma_i = 1.8$ (right).

To generate a steady cooling-film flow, the plenum chamber is supplied with a controlled mass flow such that the static pressure at the nozzle outlet equals the static pressure of the freestream flow in the wind tunnel test section at the point of injection. The controlled mass flow is generated by a choked Venturi nozzle, and a heat exchanger upstream of the Venturi nozzle controls the total temperature of the cooling fluid. Downstream of the Venturi nozzle, the flow passes through two DEHS seeding generators with 6 Laskin nozzles each. A bypass enables to control the seeding density without changing the overall mass flow rate of the cooling-film flow. With this setup, the mass flow rate settles within 1 s to steady state with a standard deviation of 0.5% of the set mass flow rate during a test run. The standard deviation of the static pressure inside the plenum is below 0.7% and the temperature is kept constant within ±0.2 K during each measurement.

PIV setup and data evaluation

The PIV setup consists of a Quantronix Darwin Duo 527-40-M laser and a Photron Fastcam SA5 high-speed PIV camera which are synchronized by an ILA synchronizer. The light sheet enters the wind tunnel through a window in the ceiling of the test section and is oriented vertically and parallel to the flow on the centerline of the model, see figure 2. The camera is mounted at a small angle (≈2°) to the normal of the light sheet under Scheimpflug condition to reduce aero-optical aberrations. It is equipped with a 180 mm Tamron tele macro lens and records a field of view of 20 mm x 20 mm in the measurement plane. In the current setup, the PIV system records 1000 samples per second with a resolution of 1024 x 1024 px². To reduce the amount of laser light scattered from the model surface into the camera, the surface is highly polished. In addition to the seeding of the cooling flow, the main flow is also seeded with DEHS. The seeding in the main flow is filtered using a cyclone particle separator that reduces the mean particle diameter. The particle response time of the tracers in the main flow is $\tau_p = 2.6\ \mu s$ and the corresponding effective mean particle diameter is $d_p = 0.7\ \mu m$. The resulting relaxation length of the particles in the freestream flow for small velocity changes is $l_p = 1.5\ mm$. Accordingly, the particle response time of the seeding in the cooling flow without the cyclone separator is $\tau_{p,i} = 7.1\ \mu s$ and $d_{p,i} = 1.2\ \mu m$, respectively. The relaxation length of the particles in the cooling-film flow is $l_p = 2.9\ mm$.

Each measurement consists of 1000 snapshots recorded over 1 s. After subtraction of a background image, the particle images are preprocessed using a non-linear Gaussian blur to reduce camera noise. The image evaluation uses an iterative correlation scheme with sub-pixel accurate image deformation. The window size used for PIV evaluation is 48 x 48 px² with 75% overlap corresponding to a physical size of 1 mm x 1 mm. This leads to a final vector resolution of 0.25 mm. Since the surface reflections were masked in the recorded images, the first point used for PIV interrogation is at $\Delta y = 0.25\ mm$ off the wall. Outliers in the vector field are determined using a normalized median test (Westerweel 2005), resulting in a validation rate over 90% in the final dataset.

Since the field of view is approx. 20 mm x 20 mm in the current setup and the cooling-film flow evolves over a considerably greater length, the results for each set of flow parameters is composed of up to nine separate measurements along the centerplane of the model. The bounds of each measurement are indicated by thin black lines in the final vector fields.

The small field of view and the high velocities of up to 600 m/s require pulse distances of 1000 ns or less. Hence, the relatively long laser pulse width of 210 ns introduces a significant amount of particle blur in the recorded particle images. Additionally, due to slight differences in the temporal pulse shape of both laser cavities, the effective pulse distance differs up to ±40 ns from the set pulse distance. This systematic error, which can be as high as 4% in the current measurements, has to be accounted for. To reduce this error, each measurement is conducted twice, where the cavities are triggered in reverse order between the measurements. With this approach, the systematic error occurs with inversed sign in both measurements such that it vanishes.

The measured velocities $\vec{U}_{12}$ for the cavity sequence 1-2 and $\vec{U}_{21}$ for the cavity sequence 2-1 can be expressed as

$$\vec{U}_{12} = \frac{\Delta\vec{s}}{\Delta t} = \frac{\vec{U}\cdot(\Delta t + \widetilde{\Delta}t_2 - \widetilde{\Delta}t_1)}{\Delta t} = \frac{\vec{U}\cdot\left(\Delta t + \widetilde{\Delta}t\right)}{\Delta t}$$

$$\vec{U}_{21} = \frac{\Delta\vec{s}}{\Delta t} = \frac{\vec{U}\cdot(\Delta t + \widetilde{\Delta}t_1 - \widetilde{\Delta}t_2)}{\Delta t} = \frac{\vec{U}\cdot(\Delta t - \widetilde{\Delta}t)}{\Delta t} \qquad \text{,with } \widetilde{\Delta}t = \widetilde{\Delta}t_2 - \widetilde{\Delta}t_1.$$

Karlsruhe, Germany, ISBN 978-3-9816764-2-6

The quantity $\vec{U}$ denotes the velocity of the flow, $\widetilde{\Delta}t_1$ and $\widetilde{\Delta}t_2$ are the effective delays of laser cavities 1 and 2, and Δt represents the set pulse distance between the triggers of the two cavities. Since the velocity $\vec{U}$ is supposed to be the same in both cases, the pulse distance error $\widetilde{\Delta}t$ can be determined when $\vec{U}_{12}$ and $\vec{U}_{21}$ are known by minimizing

$$\left\| \frac{\vec{U}_{12}}{1+\frac{\widetilde{\Delta}t}{\Delta t}} - \frac{\vec{U}_{21}}{1-\frac{\widetilde{\Delta}t}{\Delta t}} \right\|_2$$

In theory, a constant relative pulse distance error $\widetilde{\Delta}t/\Delta t$ over the measured field of view should correct a pure timing error. In practice, the corrected velocities from both cavity sequences show systematic differences towards the edge of the field of view. This could be explained by a slightly misaligned laser beam overlap in spanwise direction, where particles closer to or further away from the camera are illuminated, depending on the laser cavity. To compensate this, a two-dimensional polynomial of third degree is used for $\widetilde{\Delta}t/\Delta t$, whose coefficients are optimized in a non-linear least squares fit over the entire field of view.
The uncertainty of the pulse distance correction is estimated as the root mean square difference between the local fit for each data point and the global optimization. To compute a conservative estimation of this uncertainty, a constant relative pulse distance error $\widetilde{\Delta}t/\Delta t$ is calculated in the global optimization instead of using the polynomial function in this procedure. A typical value of the uncertainty in the pulse distance error is in the range of 2-4 ns.

Results

In this study, a cooling-film flow with an injection Mach number of $Ma_i = 1.8$ is investigated with and without shock interaction. The cooling film is injected beneath a turbulent boundary layer with a freestream Mach number of $Ma_\infty = 2.45 \pm 0.03$ and a Reynolds number based on the slot height S of $Re_S = u_0 S/\nu_0 = 41.6 \cdot 10^3 \pm 2.9\%$. The inflow boundary layer possesses a thickness of $\delta_{99}/S = 2.0$ at the point of injection. The boundary layer profiles of the mean streamwise velocity, the streamwise and wall-normal velocity fluctuations, and the Reynolds shear stress have been validated against DNS data of Pirozzoli & Bernardini (2011, 2013). A fully turbulent inflow boundary layer has been confirmed. The total temperature ratio between the cooling flow and the main flow is $T_{0,i}/T_0 = 1.00 \pm 0.8\%$ leading to a blowing rate of $M = \rho_i u_i/\rho_0 u_0 = 0.636$ and an injection Reynolds number based on the slot height of $Re_i = u_i S/\nu_i = 20.7 \cdot 10^3$. The shock is generated by a flow deflection of $\beta = 5°$ resulting in a shock angle of $\sigma = 28°$ and a static pressure ratio across the shock of $p_2/p_1 = 1.37$. The shock impinges upon the bottom wall at $x_{imp}/S = 15$. The parameters of the two flow configurations that are analyzed in this study are summarized in table 1.

Table 1: Flow parameters

			Shock strength			Injection flow		Blowing rate
Case	Ma_∞	$\frac{x_{imp}}{S}$	β [°]	σ [°]	$\frac{p_2}{p_1}$	Ma_i	Re_i	$M = \frac{\rho_i u_i}{\rho_\infty u_\infty}$
I	2.45	-	-	-	-	1.8	$20.7 \cdot 10^3$	0.636
II	2.45	15	5	28.0	1.37	1.8	$20.7 \cdot 10^3$	0.636

In the following, the case without shock interaction is denoted as case I, whereas the case with shock interaction is called case II. The results are normalized by the freestream velocity u_0, which is calculated from the wind tunnel Mach number and the total temperature. De-

Karlsruhe, Germany, ISBN 978-3-9816764-2-6

pending on the ambient conditions, the freestream velocity is in the range of $u_0 = 560 - 566\,\mathrm{m/s}$ with an uncertainty of $\pm 0.6\%$.
The error bars given in the results include random and bias errors. The estimation of the bias error includes the uncertainty in the pulse distance, the uncertainty of the freestream velocity for normalized values, and an estimated PIV noise of 0.1 px for the velocity fluctuations. The random error consists of the statistical uncertainties at a 95% confidence level. A typical value for the total error of the mean velocity is approx. 0.7% of the freestream velocity.
In figure 4, the normalized mean streamwise velocity $\bar{u}/u_0$ (figure 4a) and the normalized Reynolds shears stress $\overline{u'v'}/u_0^2$ (figure 4b) in the centerplane of the model are shown for the case I. The isoline of $Ma = 1$, calculated under the assumption that the flow is adiabatic, is superimposed. The distribution of the mean velocity (figure 4a) shows the undisturbed development of the boundary layer on the bottom wall. The distribution of the normalized Reynolds shear stress $\overline{u'v'}/u_0^2$ in figure 4b shows negative values in the boundary layer indicating the turbulent character of the boundary layer on the bottom wall. In the range $0 < x/S < 8$, the turbulent transport in the shear layer is disturbed by the expansion waves and shock waves emerging from the nozzle lip. Further downstream, the Reynolds shear stress in the shear layer becomes weaker.

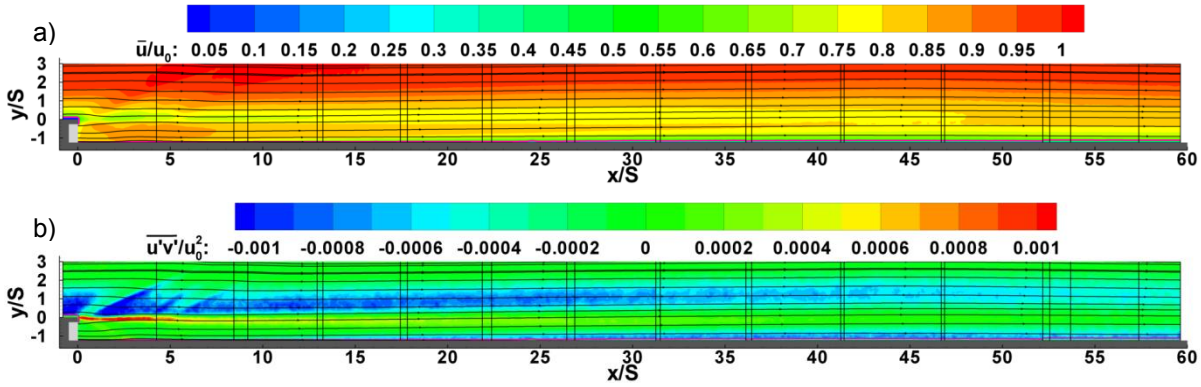

Fig. 4: Contours of the normalized mean streamwise velocity $\bar{u}/u_0$ (a) and the normalized Reynolds shear stress $\overline{u'v'}/u_0^2$ (b) for the case without shock interaction (case I).

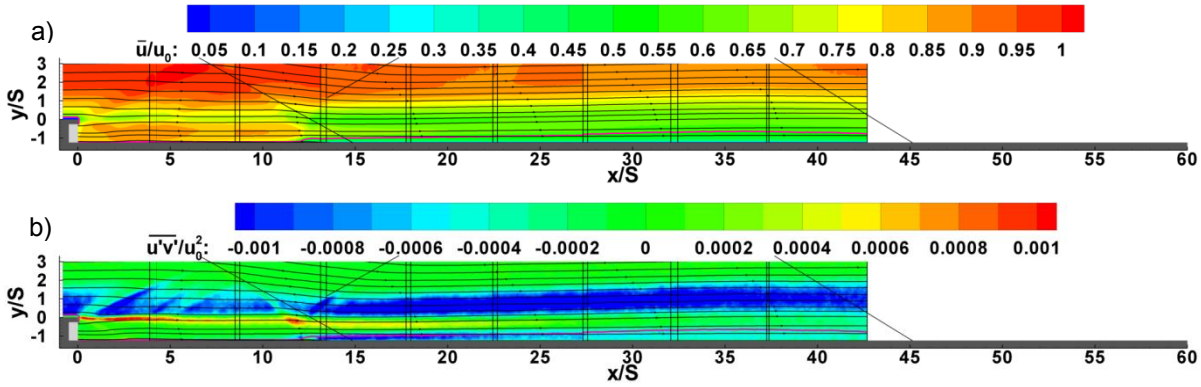

Fig. 5: Contours of the normalized mean streamwise velocity $\bar{u}/u_0$ (a) and the normalized Reynolds shear stress $\overline{u'v'}/u_0^2$ (b) for the case with shock interaction (case II).

The normalized mean streamwise velocity $\bar{u}/u_0$ and the normalized Reynolds shear stress $\overline{u'v'}/u_0^2$ for case II, i.e., with shock interaction, are shown in figure 5. The incident shock, the reflected shock, and the expected start of the expansion fan indicated by thin black lines in the plots. The impinging shock causes the formation of a subsonic layer at $x/S = 12$ that possesses an initial thickness of $y/S = 0.25$. Further downstream, the subsonic region extends to a maximum thickness of $y/S = 0.65$ at $x/S = 36$. The incident shock is reflected in

the mixing layer at approx. $y/S = 0$. The absolute value of the Reynolds shear stress in the shear layer, the mixing layer, and the slot boundary layer increases significantly downstream of the shock interaction. The Reynolds shear stress in the shear layer is increased by about 70% throughout the entire measurement range, whereas the increased Reynolds shear stress in the mixing layer and the slot boundary layer decays further downstream.
In figure 6, the peak value of the Reynolds shear stress in the slot boundary layer is plotted over x/S for both cases. Starting from $x/S = 2$, an intense positive and a negative peak of the Reynolds shear stress occur. These peak are located at a position downstream of the nozzle where the lip-expansion waves and the lip shock are expected to impact upon the bottom wall. The increase of the absolute Reynolds shear stress value directly downstream of these peaks gives strong evidence that the transition of the slot boundary layer is triggered by the lip-shock wave in both cases. Without shock interaction, the absolute Reynolds shear stress increases to a value of about $\overline{u'v'}/u_0^2 = -0.00075$ in the range $x/S > 30$. In the case with shock interaction, a negative peak of the Reynolds shear stress with a value of $\overline{u'v'}/u_0^2 = -0.0015$ arises at $x/S = 13.3$. The aforementioned decay of the Reynolds shear stress in the slot boundary layer leads to a weaker turbulent transport in the range $x/S > 26$ in the case with shock interaction compared to the no-shock configuration.

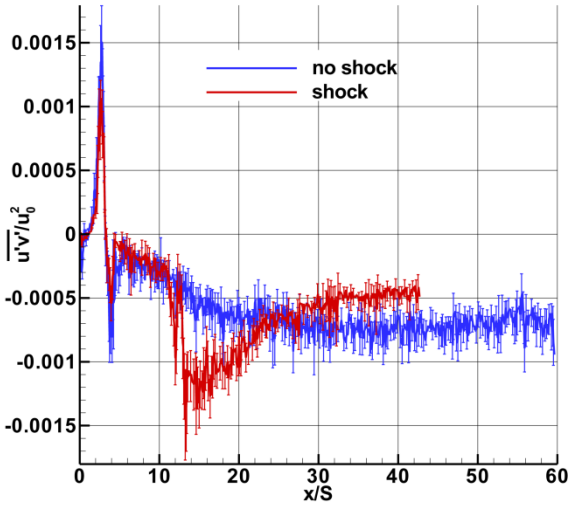

Fig. 6: Peak Reynolds shear stress $\overline{u'v'}/u_0^2$ in the slot boundary layer for case I and case II.

Wall-normal profiles of the normalized mean velocity $\bar{u}/u_0$ and the normalized Reynolds shear stress $\overline{u'v'}/u_0^2$ for both cases are shown in figure 7. The profiles are extracted at the positions $x/S = 10$, 20, and 40, thus directly upstream and downstream of the shock impingement and further downstream where the flow recovers. At $x/S = 10$, the mean velocity profile of the no-shock configuration shows the wake of the lip in the mixing layer at about $y/S = 0$. In this region, the Reynolds shear stress changes from the negative values in the shear layer to positive values in the lower part of the mixing layer. The slot boundary layer is apparent in the range $y/S < -0.9$, and is characterized by a decreasing mean velocity and negative values of the Reynolds shear stress towards the wall. Between the boundary layer and the mixing layer, the potential core is located in the range $-0.9 < y/S < -0.5$, where the Reynolds shear stress is approximately zero. The flow below $y/S = 1$ is not influenced by the impinging shock wave and the profiles of the mean velocity and the Reynolds shear stress of both cases coincide. Further off the wall, the shock is apparent by a reduced mean velocity and a local reduction of the Reynolds shear stress at $y/S = 1$.
At $x/S = 20$, the slot boundary layer and the mixing layer have merged. With shock interaction, the mean velocity profile and the Reynolds shear stress profile are compressed in the y-direction due to the flow deflection towards the wall across the shock. Hence, the peaks of

the Reynolds shear stress in the shear layer and the mixing layer are shifted towards the wall. Additionally, the magnitude of the Reynolds shear stress in the shear layer is increased by about 70%. In the cooling-film flow, shock interaction leads to a decrease of the mean velocity of about 20%, whereas the Reynolds shear stress near the wall increases.

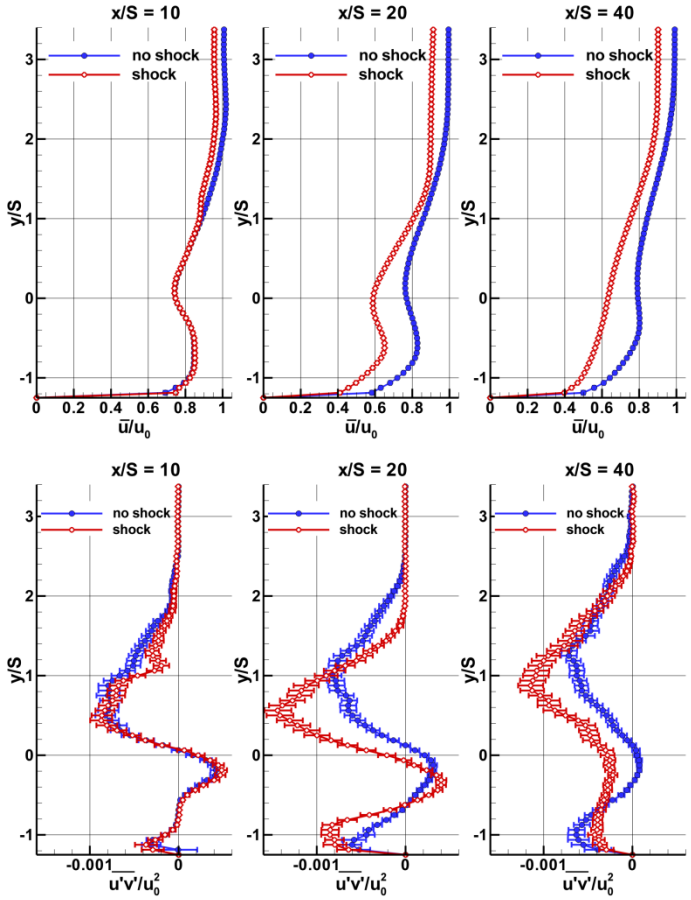

Fig. 7: Wall-normal profiles of the normalized mean streamwise velocity $\bar{u}/u_0$ and the normalized Reynolds shear stress $\overline{u'v'}/u_0^2$ at $x/S = 10, 20$ and 40 for case I and case II.

Further downstream, at $x/S = 40$, the peak Reynolds shear stress near the wall has decreased for the case with shock interaction in comparison to the case without shock. However, further off the wall in the range $-0.6 < y/S < 1.8$, the absolute value of the Reynolds shear stress with shock interaction is still higher than that without shock. The increased turbulent transport caused by the shock impingement also impacts the mean velocity. The profiles at $x/S = 40$ show a turbulent boundary layer shape in the case with shock interaction.

Conclusion

In the present study, supersonic slot-film cooling with and without shock/cooling-film interaction has been investigated using high-speed PIV measurements. A laminar cooling film is injected tangentially with an injection Mach number of $Ma_i = 1.8$ beneath a turbulent boundary layer with a freestream Mach number of $Ma_\infty = 2.45$. The inflow boundary layer has a thickness of 2.0 nozzle heights at the point of injection. In the case with shock interaction, a shock wave, generated by a wedge with $\beta = 5°$, impinges upon the cooling film 15 nozzle heights downstream of the injection point.

The laminar slot boundary layer on the bottom wall undergoes transition triggered by the lip-expansion waves and the lip shock at about $x/S = 2$. Without shock interaction, the growing slot boundary layer and the mixing layer merge at approx. $x/S = 20$ indicating the end of the potential-core region. With shock interaction, the turbulent transport in the shear layer is greatly increased downstream the shock impingement position. Near the wall, the Reynolds shear stress is locally increased at the shock impingement position and decays further downstream to values less than those of the no-shock configuration. However, the Reynolds shear stress remains at larger values compared to the case without shock interaction in the range $-0.6 < y/S < 1.8$. The intense shock-induced mixing accelerates the relaxation of the cooling-film flow, leading to a more boundary layer like velocity profile.

Acknowledgments

This research is funded by the Deutsche Forschungsgemeinschaft within the research project “Experimental Investigation of Turbulent Supersonic Film-Cooling Flows”.

References

Alzner, E., Zakkay, V., 1971: “Turbulent Boundary-Layer Shock Interaction with and without Injection”, AIAA J, Vol. 9, No. 9, pp. 1769-1776

Holden, M., Nowak, R., Olsen, G. & Rodriguez, K., 1990: “Experimental Studies of Shock Wave/Wall Jet Interaction in Hypersonic Flow”, 28th Aerospace Science Meeting, Reno, AIAA Paper, 90-0607

Juhany, K., 1994: “Supersonic Film Cooling Including the Effect of Shock Wave Interaction”, Ph D Thesis, California Institute of Technology Pasadena, California

Juhany, K., Hunt, M., 1994: “Flowfield Measurements in Supersonic Film Cooling Including the Effect of Shock-Wave Interaction” AIAA J, Vol. 32, No. 3, pp. 578–585

Kamath, P., Holden, M. & McClinton, C., 1990: “Experimental and Computational Study of the Effect of Shocks on Film Cooling Effectiveness in Scramjet Combustors”, AIAA/ASME 5th Joint Thermophysics and Heat Transfer Conference, Seattle, AIAA Paper, pp. 1190-1713

Kanda, T., Ono, F., Saito, T., Takahashi, M. & Wakamatsu, Y., 1996: “Experimental Studies of Supersonic Film Cooling with Shock Wave Interaction”, AIAA J, Vol. 34, No. 2, pp. 265-271

Kanda, T. & Ono, F., 1997: “Experimental Studies of Supersonic Film Cooling with Shock Wave Interaction (II)” J Thermophys Heat Transfer, Vol. 11, No. 4, pp. 590-592

Konopka, M., Meinke, M. & Schröder, W., 2012: “Large-eddy simulation of shock-cooling-film interaction”, AIAA J, Vol. 50, No. 10, pp. 2102-2114

Konopka, M., Meinke, M. & Schröder, W., 2013a: “Large-eddy simulation of shock-cooling-film interaction at helium and hydrogen injection”, Phys Fluids, Vol. 25, 106101

Konopka, M., Meinke, M. & Schröder, W., 2013b: “Large-eddy simulation of high Mach number film cooling with shock-wave interaction”, Progress in Flight Physics 5, pp. 309-326, doi:10.1051/eucass/201305309

Olsen, G., Nowak, R., Holden, M. & Baker, N. R., 1990: “Experimental Results for Film Cooling in 2-d Supersonic Flow Including Coolant Delivery Pressure, Geometry, and Incident Shock Effects”, 28th Aerospace Science Meeting, Reno, AIAA Paper, 90-0605

Pirozzoli, S., Bernardini, M., 2011: “Turbulence in supersonic boundary layers at moderate Reynolds number”, J Fluid Mech, Vol. 688, pp. 120-168

Pirozzoli, S., Bernardini, M., 2013: “Probing high-Reynolds-number effects in numerical boundary layers”, Phys Fluids, Vol. 25, 021704

Seban, R. A., Back, L. H., 1962: “Velocity and Temperature Profiles in Turbulent Boundary Layers with Tangential Injection”, J Heat Transfer, Vol. 84, pp. 45-54

Westerweel, J. & Scarano, F., 2005: “Universal outlier detection for PIV data”, Exp Fluids, Vol. 39, pp. 1096-1100